On the Effect of Non-Carbon Nanostructured Supports on the Stability of Pt Nanoparticles during Voltage Cycling: a Study of TiO2 Nanofibres

Iuliia Savych, Julien Bernard d'Arbigny, Surya Subianto, Sara Cavaliere, Deborah Jones, Jacques Rozière

▶ **To cite this version:**

Iuliia Savych, Julien Bernard d'Arbigny, Surya Subianto, Sara Cavaliere, Deborah Jones, et al.. On the Effect of Non-Carbon Nanostructured Supports on the Stability of Pt Nanoparticles during Voltage Cycling: a Study of TiO2 Nanofibres. Journal of Power Sources, 2014, 257, pp.147-155. 10.1016/j.jpowsour.2014.01.112 . hal-00944222

HAL Id: hal-00944222
https://hal.science/hal-00944222

Submitted on 10 Feb 2014

HAL is a multi-disciplinary open access archive for the deposit and dissemination of scientific research documents, whether they are published or not. The documents may come from teaching and research institutions in France or abroad, or from public or private research centers.

L'archive ouverte pluridisciplinaire **HAL**, est destinée au dépôt et à la diffusion de documents scientifiques de niveau recherche, publiés ou non, émanant des établissements d'enseignement et de recherche français ou étrangers, des laboratoires publics ou privés.

On the Effect of Non-Carbon Nanostructured Supports on the Stability of Pt Nanoparticles during Voltage Cycling: a Study of TiO_2 Nanofibres

I. Savych, J. Bernard d'Arbigny, S. Subianto, S. Cavaliere*, D. J. Jones, J. Rozière

Institut Charles Gerhardt, UMR CNRS 5253,

Agrégats Interfaces Matériaux pour l'Energie, Université Montpellier 2

34095 Montpellier Cedex 5, France

* Institut Charles Gerhardt, UMR CNRS 5253, Laboratoire des Agrégats Interfaces et Matériaux pour l'Energie, Université Montpellier 2 -34095 Montpellier Cedex 5, France. Fax: +33 (0)4 67 14 33 04; Tel: +33 (0)4 67 14 90 98; E-mail: sara.cavaliere@univ-montp2.fr

Abstract

Electrospun carbon and Nb-doped TiO_2 nanofibres (CNFs, TNFs) have been investigated as electrocatalyst supports for polymer electrolyte membrane fuel cells (PEMFC). The optimal Nb doping amount has been identified for TNFs, and thermal treatment of titanium oxide fibres optimised to balance the surface area and electronic conductivity requirements. The most highly conducting material is characterised by a high concentration of surface Ti^{3+} and Nb^{4+} (and oxygen vacancies). Pt nanoparticles of average diameter of 2.3 nm were loaded onto 10 $\%_{at}$ Nb doped-TiO_2, retained as the best candidate for further electrochemical analysis, and on CNFs, using a microwave-assisted polyol method. Significantly higher electrochemically active surface area was retained after voltage cycling to 1.2 V for Pt supported on TNF (73 %) than on CNFs, where only 8% of the original ECSA was conserved after 1000 voltammetric cycles. The mass activity was also slightly higher for the titanium oxide based electrodes in the oxygen reduction reaction.

Keywords: alternative electrocatalyst support, titania, nanofibres, PEMFC, electrospinning.

1. Introduction

One of the major issues concerning the durability of Proton Exchange Membrane Fuel Cells (PEMFC) is electrode degradation over time [1]. In this respect, the electrocatalyst support material plays a very crucial role [2]. It is known that conventional carbon black-based supports, although having excellent electrical conductivity and high surface area, suffer from corrosion at the cathode under operation conditions leading to cell reversal according to equation (1) [3]: $C + 2H_2O \rightarrow CO_2 + 4H^+ + 4e^-$ $E^0 = 0.207$ V (1)

High temperature and humidity contribute to accelerate this phenomenon [4]. Such degradation leads to the aggregation and migration of the noble metal catalysts and even their detachment from the support surface with a loss of the electroactive surface area of the electrode [5].

Recent years have witnessed a growing interest in conductive nanotubes and nanofibres as catalyst supports for PEMFC electrodes, due to the impact of their nanostructure and morphology on performance and durability. Comparative studies on carbon black and carbon fibres showed that the latter demonstrate better resistance to electrochemical corrosion, which was attributed to the more graphitic microstructure of the nanofibres [6]. Furthermore, their one dimensional morphology and the sub-micron scale can provide a high surface area and directional electronic transport, while also offering the possibility of promoting catalyst dispersion leading to enhanced electrocatalytic performance [7]. In this regard, electrospinning is a versatile technique for synthesis of nanofibrous materials with uniform and controlled diameters and structures [8, 9], which in the past few years has developed as an emerging fabrication method for fuel cell electrocatalyst supports and electrodes [10, 11]. The most widely used method in the preparation of carbon fibres by electrospinning is by controlled thermal treatment of polyacrylonitrile (PAN) electrospun fibres [12]. This type of carbon nanofibre (CNF) is finding use as catalyst support both for direct methanol fuel cell anodes,

where improved performance compared to commercial electrocatalysts has been reported [13, 14], and in PEMFC [15, 16].

Another approach to avoid corrosion issues in fuel cell electrodes is the partial or total replacement of carbon with alternative support materials, including semi-conductor oxides (TiO_x, WO_x, SnO_2, etc…) or carbides [17-20]. Indeed, these materials may not only improve corrosion resistance, but can also promote electrocatalysis through synergetic metal-support interactions [21]. However, semi-conducting oxides such as TiO_2 also presents a drawback compared to carbon in that pure TiO_2 is a semiconductor with a band gap of 3.2 eV for anatase and 3.0 eV for rutile [22], and therefore the challenge is to develop strategies to enhance the inherent electronic conductivity. Two main strategies exist in this regard: Firstly, doping with donor-type ions such as Mo^{6+} or Nb^{5+} modifies the electrical structure, allowing an easier electron transport [23-26]. Secondly, sub-stoichiometric titanium dioxide with oxygen vacancy-induced conductivity can be prepared by thermal treatment in a reducing atmosphere [27-29]. Another alternative consists of the preparation of composites based on the combination of TiO_2 with conducting materials (*e.g.* carbon) [30, 31]. Indeed, despite the lower conductivity relative to carbon, TiO_2 is a promising support material as their catalysed forms have been shown to have oxygen reduction reaction (ORR) activity similar to that of conventional Pt/C catalysts, but with greater stability and activity retention after accelerated stress tests, in *ex situ* as well as in fuel cell experiments [23, 29, 32, 33].

TiO_2-based nanofibres obtained by electrospinning have recently been used as fuel cell electrocatalyst supports, with Pt nanoparticles deposited on pure titanium dioxide fibres by microwave irradiation showing better activity towards methanol oxidation than commercial Pt/C [34]. More conductive electrospun oxides, such as Nb doped TiO_2, TiO_x [35, 36], and composite Nb-TiO_2-C [37] showed oxygen reduction reaction activity comparable to conventional carbon-based electrocatalysts with an enhanced stability as shown by greater

retention of Pt active surface area over time. Electrospun TiO_2 fibres can also be reduced to the Magneli phase (Ti_4O_7) in order to enhance their conductivity [38].

We report here the results of an investigation comparing the electrocatalytic properties of Pt on carbon and on Nb doped titanium dioxide based nanofibres towards oxygen reduction and their electrochemical stability on voltage cycling. The platinum nanoparticles were synthesised by a microwave polyol method [39] and deposited on fibrous electrospun supports.

2. Experimental section

2.1 Preparation of electrocatalyst supports

2.1.1 Carbon nanofibres

A 7.5 $\%_{wt}$ polyacrylonitrile (PAN, M_w = 150,000, Sigma-Aldrich) solution in N,N-dimethylformamide (DMF, 98 %, Sigma-Aldrich) was stirred at 60 °C overnight. The solution was electrospun in air with a standard syringe and a grounded rotating drum collector configuration (Linari Engineering). The distance between the needle tip and the rotating drum was 10 cm, the applied voltage 10 kV and the flow rate 0.5 mL h^{-1}. The resulting white electrospun nanofibre mat was stabilised in air at 280 °C for 1 h at a heating rate of 1 °C min^{-1}, leading to a brown material. After cooling to RT, the fibres were carbonised at 1000 °C for 1 h in a nitrogen atmosphere at a heating rate of 5 °C min^{-1} and a black final product was obtained.

2.1.2 (Nb-)TiO_2 nanofibres

A procedure similar to that in [40] was followed. Briefly, a carrier polymer solution of polyvinyl pyrrolidone (PVP, M_w ~1,300,000, Aldrich) in absolute ethanol (puriss., Sigma-Aldrich) was added to a precursor solution made of 0.52 mL of titanium(IV) isopropoxide (97 %, Aldrich), 0.04 to 0.16 mL of niobium ethoxide (99.95 %, Aldrich) (5 to 20 $\%_{at}$ doping) (both stored in a glove box) and 1 mL of acetic acid (Sigma-Aldrich). The solutions were degassed by ultrasonication for 15 min, mixed together and stirred for 1 hour and loaded into the syringe. Electrospinning in air used a distance between the needle tip and the collector plate of 10 cm,

an applied voltage of 15 kV and a 0.5 mL h^{-1} flow rate. The as-prepared fibres were calcined in air at 500 °C or 800 °C at 5 °C min^{-1} for 6 h in order to decompose and remove the carrier polymer [samples labelled respectively as LT (low temperature) and HT, high temperature)]. The LT sample, further treated at 800 °C in 5 % H_2/Ar for 2 h, is denoted HTR (high temperature with reduction treatment). The LT and HT fibres were white, whereas the HTR were blue.

2.2 Pt deposition on electrocatalyst supports

177 mg of hexachloroplatinic acid (H_2PtCl_6 $6H_2O$, 99.9 % Alfa Aesar) were dissolved in 80 mL of ethylene glycol (99.5 %, Fluka) and brought to pH 11.5 by addition of NaOH (98 %, Sigma Aldrich). The resulting solution was heated at 130 °C for 6 minutes under microwaves (MiniFlow 220SS Sairem) to obtain Pt nanoparticles. A suspension containing 100 mg of the support material (carbon or Nb-TiO_2 fibres) in 5 mL ethylene glycol was sonicated for 10 min and added to the Pt nanoparticle solution, brought to pH 2 by the addition of H_2SO_4 (95-98 %, Aldrich) and stirred for 24 h to allow Pt adsorption onto the support. The products were liberally washed with water and ethanol, filtered and dried in an oven at 80 °C for 24 h.

2.3 Characterisation of the prepared materials

2.3.1 Electron microscopy

The morphology of the electrospun materials was analysed by using a Hitachi S-4800 scanning electron microscope (SEM), a FEI Quanta FEG 200 and a JEOL 1200 EXII transmission electron microscope (TEM) operating at 120 kV equipped with a CCD camera SIS Olympus Quemesa (11 million pixels). For TEM analyses, the samples were suspended in ethanol and ultrasonicated before deposition onto carbon film coated copper grids.

2.3.2 X-ray diffraction

Structural characterisation was performed by X-ray diffraction on a PANAlytical X'pert powder diffractometer equipped with CuK_α radiation (λ = 1.542 Å).

2.3.3 Specific surface area determination

Nitrogen adsorption/desorption isotherms were determined at -196 °C by means of a Micromeritics ASAP 2020 apparatus after outgassing samples overnight at 200 °C. The specific surface area was calculated using the Brunauer-Emmett-Teller (BET) equation, taking the cross-sectional area of one N_2 molecule as 0.162 nm^2. The pore size distribution has been calculated by the Barret-Joyner-Halenda (BJH) method using the desorption branch of the isotherm.

2.3.4 Raman spectroscopy

Raman spectra were recorded on a LabRAM Aramis IR2 Horiba Jobin Yvon spectrometer equipped with a He/Ne laser (λ = 633 nm, 17 mW on TNFs and 4 mW on CNFs) and a long work distance objective × 50.

2.3.5 Thermogravimetric analysis

Thermogravimetric analysis was performed in air up to 800 °C (10 °C min^{-1}) using a Netzsch TG 439 thermobalance to determine the Pt loading on Pt/CNF electrospun fibres.

2.3.6 X-ray photoelectron spectroscopy

The surface composition of the Pt/Nb-TiO_2 fibres was monitored by X-ray photoelectron spectroscopy (XPS) on an ESCALAB 250 (Thermo Electron). The X-ray excitation was provided by a monochromatic Al K_α (1486.6 eV) source, and the analysed surface area was 400 μm^2. A constant analyser energy mode was used for the electron detection (20 eV pass energy). Detection of the emitted photoelectrons was performed perpendicularly to the surface sample. Data quantification was performed on the Avantage programme, removing the background signal using the Shirley method. The surface atomic concentrations were determined from photoelectron peaks areas using the atomic sensitivity factors reported by Scofield. Binding energies of all core levels are referred to the C-C bond of C 1s at 284.8 eV.

2.3.7 Electronic conductivity

The conductivity of the carbon and oxide fibres was determined as a function of temperature from measurements with an in-house cell equipped with four gold electrodes and using Van Der Pauw calculations. Samples were analysed as pellets prepared by compaction at 370 MPa for 10 min. In the case of carbon fibres, 558 mg of 5 $\%_{wt}$ Nafion® dispersion was added as a binder to 96 mg of CNFs. The mixture was oven dried at 70 °C overnight.

2.3.8 X-ray fluorescence spectroscopy

The Pt content of Nb doped TiO_2 nanofibres was determined by X-Ray fluorescence measurements with a PANalytical Axios Max spectrometer fitted with a Rh (4 kW) tube and LiF200 crystal The samples were pellets of ground fibres in a H_3BO_3 matrix (32 mm diameter) prepared by pressing at 740 MPa for 5 min. 100 mg of the titania fibres are needed to obtain a scanned surface of ca. 12 mm in diameter. Standards were prepared with TiO_2 nanopowder (Aldrich) containing 5, 10, 15 and 20 $\%_{wt}$ of Pt black (Alfa Aesar) to calibrate the signal. Omnian software was used for data analysis.

2.3.9 Electrochemical characterisation

Electrochemical analyses were carried out in a three-electrode cell comprising a gold (chronoamperometry, geometric area 0.03 cm^2) or glassy carbon (other voltammetric characterisations, geometric area 0.196 cm^2) rotating disk electrode (RDE) (working electrode), a saturated calomel electrode (reference electrode) and a platinum wire (counter electrode), and a Bio-Logic SP-150 instrument and a Pine bipotentiostat model AFCBP1. All the potential values are referred to the reversible hydrogen electrode (RHE).

Potentiostatic accelerated stress tests were performed by holding the working electrode potential at 1.4 V vs RHE for 2 hours in 0.5 M H_2SO_4 at 80 °C. The ink was prepared by dispersing 20 mg of the support material (5 $\%_{wt}$ CNF, HTR-TNF or Vulcan XC-72R) in 1 mL of ethanol (Aldrich) and 200 µL of 5 $\%_{wt}$ Nafion® dispersion (Aldrich) by ultra-sonication for

30 minutes. 3 µL of the resulting colloidal suspensions were deposited onto the RDE surface with a micropipette.

Voltammograms were recorded from measurements at room temperature on materials deposited on the glassy carbon electrodes prepared with the following procedure. 5 mg of the support material (Pt/CNFs or Pt/HTR-TNFs) were dispersed in 0.20-0.35 mL of ethanol (Aldrich), 10-25 µL of water and 10-25 µL of 5 $\%_{wt}$ Nafion® dispersion (Aldrich) by ultra-sonication for 30 minutes. 5 or 10 µL of these inks were then deposited onto the RDE surface with a micropipette. The Pt loading was 87 µg cm^{-2} for Pt/ HTR-TNFs and 131 µg cm^{-2} for Pt/CNFs.

Each electrode was cycled 10 times in N_2 purged 0.1 M $HClO_4$, sweeping in the potential range of 0.05 to 1.2 V vs RHE at a scan rate of 50 mV s^{-1} to clean the Pt surface, and the result at cycle 10 was used to determine the initial ECSA. For durability test these cycles were performed 1000 times and the ECSA was evaluated after these prolonged cycles. Its calculation was based on hydrogen desorption peaks in the range 0.05 V to 0.4 V vs RHE, assuming a hydrogen desorption charge of 210 µC cm^{-2} for the electroactive Pt surface [41].

The activity of the electrodes in the oxygen reduction reaction (ORR) was followed using linear sweep voltammetry at rotation rate from 400 to 2500 rpm in O_2 saturated 0.1 M $HClO_4$. The potential was varied from 1.0 V to 0.2 V vs RHE at a scan rate of 5 mV s^{-1}. The current density is reported here as current per geometric electrode area.

3. Results and discussion

3.1. Characterisation of electrospun carbon and Nb doped TiO_2 nanofibrous supports

Carbon obtained by electrospinning a PAN solution followed by stabilisation and carbonisation steps [42] was characterised by SEM, and the micrograph in Fig. 1a indicates that the nanofibres obtained are quite homogeneous with an average diameter of 130 nm (Fig. 1b). N_2 adsorption/desorption measurements showed that carbon fibres are microporous (type I

isotherm, see Fig. S1, Supporting Information) [43], and their BET specific surface area is 36 m^2 g^{-1}. The Raman spectrum (Fig. S2, SI) shows the two bands typical for carbonaceous materials, one centred at 1326 cm^{-1} attributed to the defect-induced mode (D-band), and one situated at 1584 cm^{-1} attributed to ordered graphitic structures (G-band). The relative intensity ratio of D-band to G-band indicates the relative content of graphite in the carbonaceous materials, with lower values corresponding to higher amount of sp^2 (graphite) clusters in the sample [44, 45]. In the present case, the D/G ratio is 1.7, showing a predominance of disordered carbon over graphite, due to the relatively low carbonisation temperature (1000 °C). The presence of the graphitic phase is demonstrated by XRD (see SI). The crystallite size is 1.3 nm as estimated by the Scherrer equation using the C_{002} diffraction line at 24.8 ° [44].

The conductivities of the CNFs and of Vulcan XC-72R as a function of temperature up to 250 °C are compared in Fig. 2 a. Although the XC-72R presents a similar conductivity to that of CNFs at RT (5.3 vs 6.2 S cm^{-1}), its conductivity shows a decreasing trend with temperature, while that of the electrospun CNFs remains at a value between 6 and 8 S cm^{-1} in the temperature range studied, corresponding to a semi-metal-like behaviour.

A study was then performed to study the effect of doping agent (at levels of 5-20 $\%_{at}$ Nb) on the electrical conductivity in titania nanofibres. Different thermal treatments (LT, 500 °C, air; HT, 800 °C, air; HTR, 800 °C 5 % H_2/Ar) were additionally used to obtain different titania structures and to induce structural defects, which also affect the electron transport. Nb^{5+} was chosen as donor type dopant because its ionic radius (0.69 Å) is similar to that of Ti^{4+} (0.64 Å) [46] and gives the possibility of isotropic dissolution in TiO_2 as Nb_2O_5 over a wide concentration range [47].

Table 1 shows the electrical conductivity and the BET surface area values for the samples prepared under these conditions. In general, samples heat-treated in air present a conductivity similar to that of pure titanium dioxide (ca. 10^{-9}/10^{-7} S cm^{-1}), while the H_2 treated

HTR samples are characterised by significantly higher conductivities, the highest observed value of $5 \cdot 10^{-3}$ S cm^{-1} being for TNF doped with 10 $\%_{at}$ Nb and calcined at 800 °C in reducing atmosphere. As depicted in Fig. 2 b, the conductivity increases with temperature following a semiconductor behaviour and at 100 °C, around the operating temperature of PEMFC, it reaches a value of $1.5 \cdot 10^{-2}$ S cm^{-1}. The sample with 10 $\%_{at}$ Nb-TiO_2 HTR was thus selected for electrocatalyst deposition and further electrochemical characterisation. It is interesting to note that the BET surface area increases with increasing Nb doping level. This feature is especially evident for LT treated fibres, which show surface area of 30, 50, 70 and 87 m^2 g^{-1} for 0, 5, 10 and 20 $\%_{at}$ Nb doping, respectively. This result may be attributed to the reduction in the size of the grains forming the nanofibres that increases the developed surface of the materials. This is in agreement with analysis of XRD data of LT samples using the Scherrer equation, which provides a calculated domain size of 15, 12, 8 and 9 nm for 0, 5, 10 and 20 $\%_{at}$ Nb doping, respectively. The effect of niobium on inhibiting titania grain growth is well known [24, 47-49], and our results confirm that this effect is also present in electrospun titania nanofibres.

The nitrogen adsorption/desorption isotherms (see SI) indicated that the LT sample is mesoporous (type IV + I isotherm [43]) and presents a narrow pore size distribution with an average pore diameter of 6 nm, whereas HT and HTR samples only possess intergrain porosity. The specific surface area of HT and HTR samples are lower than for samples treated at low temperature with a decrease from 65 to 20 m^2 g^{-1}, due to particle sintering effects [50] which are clearly observable by electron microscopy. Although the diameter of the fibres of LT and HTR samples is similar, *ca* 50 nm (20 - 120 nm), LT fibres are made up of nanoparticles of *ca*. 10 nm in size, whereas HTR fibres are comprised of nanoparticles of around 50 nm (Fig. 3).

The calcination temperature also affects the crystal structure of the TNF. At 500 °C, the main phase observed is anatase, as revealed by XRD (JCPDS 01-084-1285) in Fig. 4 a, although the weak diffraction line at 27.5 ° 2 theta indicates the presence of a very minor amount of rutile

as well. In contrast, the X-ray diffraction pattern of Fig. 4 b indicates that TiO_2 HTR is principally in the rutile form (JCPDS 01-078-1510). These results are further confirmed by Raman analysis (Fig. S5 in SI, lines at 144, 398, 516, and 637 cm^{-1} for LT anatase [51] and at 415 and 600 cm^{-1} for HTR rutile [51, 52]), but nevertheless, even after the HT treatment, a non-negligible amount of non-converted pristine anatase is still present (diffraction line at 25.3 ° 2 theta) due to Nb inhibiting the anatase to rutile phase transition, explaining the presence of anatase even after heat treatment at 800 °C [47]. No evidence for segregated Nb_2O_5 phase was detected at any of the doping levels investigated, implying that the doping of Nb into the TiO_2 lattice was effective. At high doping levels (20 $\%_{at}$ Nb), a small amount of titanium niobium oxide $2TiO_2 \cdot 5Nb_2O_5$ (JCPDS: 00-040-0039) is also present in the HT sample (see SI). The insertion of Nb^{5+} into the TiO_2 lattice is further corroborated by the progressive shift to lower angles of XRD lines at progressively increasing level of Nb (from 25.4 to 25. 2 ° for anatase and from 27.4 to 27.2 ° for rutile samples), indicating an increase of the unit cell volume in agreement with the difference of the ionic radii of Nb^{5+} (0.69 Å) and Ti^{4+} (0.64 Å) [46] (see SI). Surprisingly, no TiO_x suboxide was detectable by X-ray diffraction of the HTR nanofibres despite their high electronic conductivity and their blue colour. It is likely that only a small amount of the sample, below the detection limit of XRD (i.*e.* the fibre surface in contact with the reducing gas at high temperature), was effectively reduced and converted to suboxide In order to substantiate this, a surface composition analysis was performed by XPS.

High resolution spectra of the HTR fibres in the binding energy regions of Ti 2p and Nb 3d are characterised by broader lines when compared to the spectra given by LT and HT fibres (see SI, Fig. S10-S12). The peak position of Ti $2p_{3/2}$ A , at 459.2 eV, corresponds to that of Ti^{4+} oxidation state [53], as expected for stoichiometric TiO_2, and also as reported in the literature for LT treated Nb-doped titania fibres [40]. A second contribution (60 $\%_{at}$ of the total titanium), not observed for the other (LT, HT) samples, appears at 457.8 eV (Ti $2p_{3/2}$ B), and can be

attributed to titanium in the oxidation state +3 [54]. This shows that the presence of Ti^{3+} and the associated oxygen vacancies is at the origin of the enhanced conductivity of the HTR samples. We can therefore conclude that the sample treated at high temperature under H_2/Ar is mainly rutile-type titanium dioxide in the bulk fibre, with a sub-oxide TiO_{2-x} at the surface.

3.2. Electrochemical characterisation of the nanofibrous supports

Since the corrosion of the carbon support is the main driving force of catalyst degradation, it was quantified by electrochemical oxidation (accelerated experiments) at 1.2 V RHE for 24 h or 1.4 V RHE for 2 h. The first potential of 1.2 V RHE represents the thermodynamic potential limit of PEMFC operation under normal conditions, whereas corrosion resistance was assessed at a potential of 1.4 V RHE which is close to the cathode potential in the conditions of fuel starvation and reverse current at which the corrosion of the support is most prominent [55]. Both carbon black (Vulcan XC-72R) and CNF were analysed for comparison with the TNF support, and the electrochemical degradation was estimated in terms of loss or modification of the CNF and TNF supports from the integrated corrosion current [56] as compared to the value obtained for Vulcan XC-72R [57].

The LT and HR niobium doped titania, even when catalysed with Pt nanoparticles, presented lower electrocatalytic performance than the HTR material, which is consistent with the relative conductivity of these samples. All successive electrochemical characterisation was therefore limited to the 10 $\%_{at}$ Nb-TiO_2 HTR (HTR-TNFs). Comparison of the oxidation currents at high potential for the titanium dioxide and the carbon-based materials is made in Fig. 5. Indeed, the carbon material shows a larger corrosion current than the one recorded on TiO_2 fibres, reflecting its corrosion behaviour *i.e.* the oxidation of carbon to CO_2 [58]. The integrated charges for Vulcan XC-72R, CNFs, and HTR-TNFs were respectively 3.9, 5.6, 0.9 and C mg^{-1}, showing that titanium dioxide based material has a smaller corrosion charge and

thus higher electrochemical stability than both carbon nanofibres and carbon black at high potential.

3.3. Characterisation of catalysed fibrous supports

Transmission electron microscopy was used to characterise the Pt deposited by the microwave-assisted polyol method on CNFs and HTR-TNFs. On the CNF surface, the Pt particles are well dispersed with an average diameter of 2.3 nm (Fig. 6 a and c) a Pt loading of 18 $\%_{wt}$ as indicated by thermogravimetric analysis. Similarly, and as shown in Fig. 8 a and c, the dispersion of the Pt particles is homogeneous all over the HTR-TNF surface with the same average diameter of 2.3 nm and a similar Pt loading of 16 $\%_{wt}$ (determined by X-Ray Fluorescence).

3.4. Electrochemical characterisation of catalysed fibrous supports

Cyclic voltammetry (CV) measurements on the catalysed supports (Pt/CNFs and Pt/HTR-TNFs, Fig. 7) show characteristic hydrogen adsorption/desorption peaks in the potential range of 0.05-0.4 V vs RHE as well as Pt oxide formation (> 0.8 V) and reduction (0.5 - 1 V). The catalyst electrochemical surface area (ECSA) was calculated from the hydrogen desorption peak in each case, and had a value of 36 $m^2\ g^{-1}$ for Pt on HTR-TNFs and 24 $m^2\ g^{-1}$ for Pt on CNFs. The electrodes were each then cycled 1000 times between 0.05 and 1.2 V vs RHE and the ECSA recalculated in order to assess their respective stability to high potential. A decrease of the active Pt area was observed for both samples with increasing number of cycles, as indicated by a decrease in the integrated area of the hydrogen desorption peaks. Nevertheless, the degradation over time is notably stronger for the carbon supported sample than with the TNF support. Indeed, the electroactive area of Pt/CNFs decreased much faster with cycling than with Pt/HTR-TNFs: after 500 cycles Pt/CNFs lost 81 % of the ECSA and 92 % after 1000 cycles, while Pt/TNFs lost 20 % and 27 % after 500 and 1000 cycles respectively (Fig. 7 and Table 2). Furthermore, an increase of the double layer region for Pt/CNFs is observed after

prolonged cycling, which may indicate corrosion accompanied by the formation of surface functional groups such as -OH and -COOH [62]. These results are in agreement with the change in size distribution of the Pt nanoparticles after cycling shown in Fig. 6 and 8, where the average particle size increased from 2.3 nm to 7.0 nm for Pt/CNFs with a wide dispersion in size up to 15 nm, but to only 5.0 nm for Pt/HTR-TNFs (Table 2). This can be explained by the corrosion of the carbon-based support during the potential cycling, leading to ripening and agglomeration of the Pt particles, for instance by the known dissolution and re-deposition mechanism [59, 60]. The Nb-doped titania supported catalyst showed a higher stability, and retained the size and the activity of the deposited nanocatalysts. This is understood both by strong Pt-metal interactions and the greater (electro)chemical stability of the ceramic support. This high resistance to corrosion is in agreement with recent reports on Nb doped titania as well as tin oxide-based supports [19, 33, 35, 50, 61]. Thus, the potential opened by pure oxide supports prepared by a simple and easily up-scalable route such as electrospinning to solve the carbon corrosion problem in PEMFC are hereby demonstrated. As oxide-based supports may also improve catalysis through specific metal-support interactions, the ORR was also Fig. 9 shows the linear sweep voltammograms recorded for Pt/HTR-TNF (a) and Pt/CNF (b). Both polarisation curves show an onset potential around 0.95 V. By using the Levich-Koutecky equation [63] for both CNF and HTR-TNF supported Pt (see SI), the number of electrons involved in the ORR was estimated close to four, indicating the complete reduction of O_2 to H_2O. The Tafel plot corresponding to the polarisation curves of Pt/CNFs and Pt/HTR-TNFs at a rotation speed of 900 rpm is depicted in Fig. 9 c. It shows that the ORR mass activities were quite similar for the two samples, but slightly higher for Pt deposited on HTR-TNFs than for Pt on CNFs. For instance, at 0.9 V the first reached a value of 2.4 A g_{Pt}^{-1}, while for the latter it was 1.7 A g_{Pt}^{-1}, *i.e.* similar to those reported on titanium oxide-based supports [33, 35]. Further improvements

on the ORR activity are needed and dedicated works on the optimisation of the nanocatalyst size and loading are in progress.

4. Conclusions

Electrospun titanium oxide nanofibres (TNF) have been used as alternative PEMFC electrocatalyst supports. They were subjected to specific thermal treatments and doped with niobium in order to achieve a high concentration of surface Ti^{3+} and Nb^{4+} (and oxygen vacancies), allowing an optimal balance of surface area and electronic conductivity requirements. Their electrochemical stability and ORR activity have been presented in comparison with carbon nanofibres (CNF). The novel Pt/TNF materials demonstrated high stability after accelerated stress tests, retaining 73 % of the electroactive Pt area, versus the 8 % of Pt/CNFs. The dramatically enhanced corrosion resistance of the titanium oxide based support is ascribed to the high chemical and electrochemical stability of the ceramic material compared to carbon as well as to the Pt-TiO_2 support-metal interaction. These nanofibrous carbon-free materials can be a promising alternative as PEMFC electrocatalysts, with the advantage of a simple and easily up-scalable preparation method such as electrospinning.

Figures and Tables

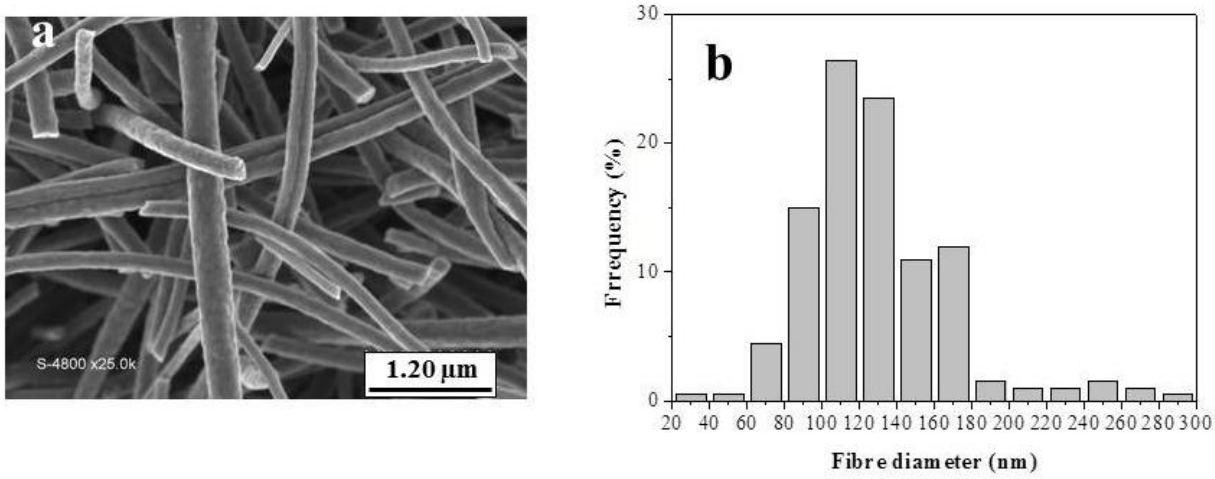

Fig. 1. Scanning electron micrograph of carbon nanofibres (a) and corresponding size distribution histogram (b).

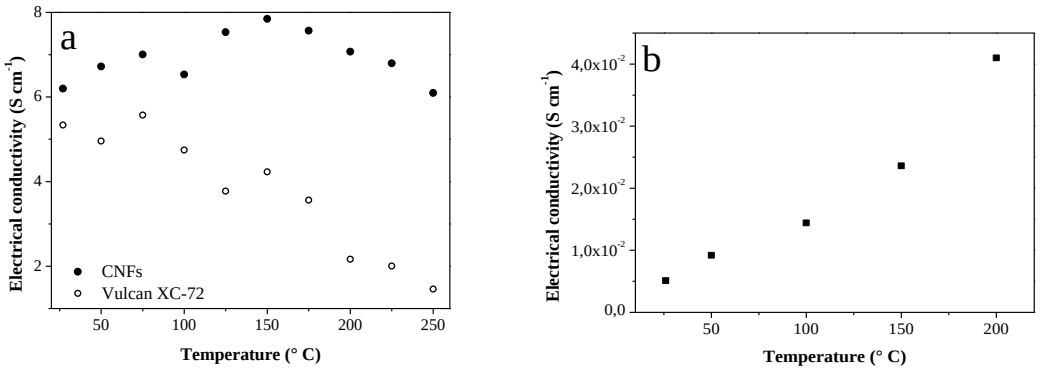

Fig. 2. Temperature dependence of the conductivity of carbon nanofibres and Vulcan XC-72R (a) and HRT 10 $\%_{at}$ Nb-TiO_2 nanofibres (b).

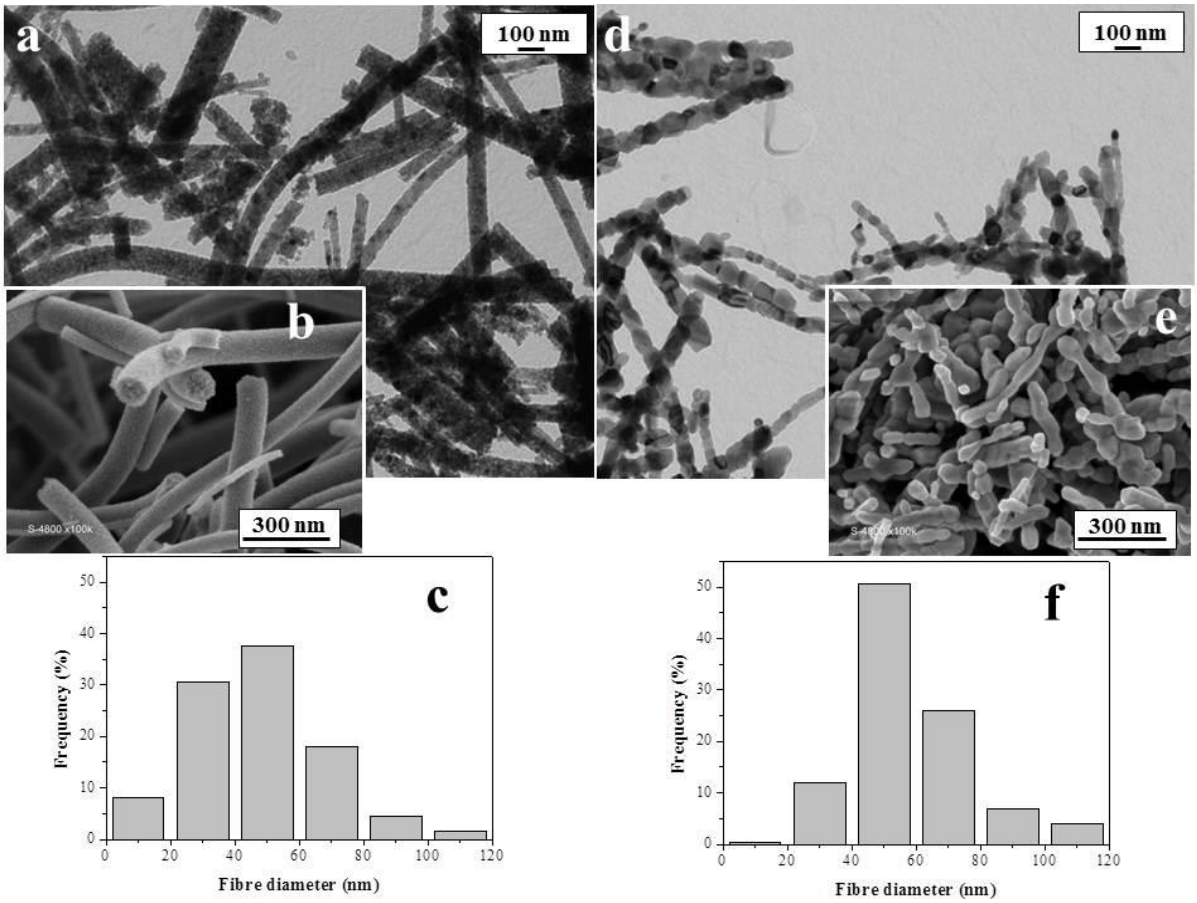

Fig. 3**.** Transmission (a, d) and scanning (b, e) electron micrographs and corresponding size distribution histograms (c, f) of 10 $\%_{at}$ Nb-TiO_2 LT and HTR fibres, respectively.

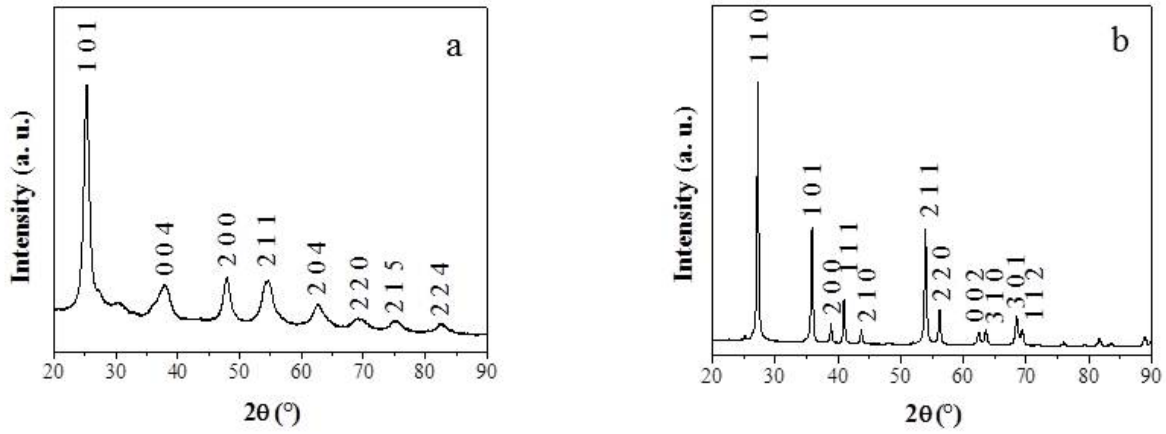

Fig. 4. XRD patterns with Miller indices of 10 $\%_{at}$ Nb-TiO_2 LT (a) and HTR fibres (b).

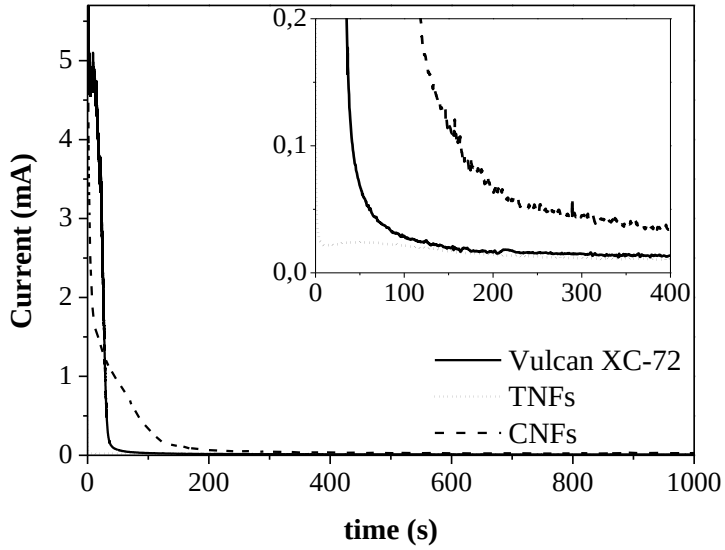

Fig. 5. Oxidation/corrosion characteristics for electrospun carbon and titanium dioxide nanofibres (CNFs and HTR-TNFs) and Vulcan XC-72R at 1.4 V vs RHE. Although the experiment was run for 2 hours, for the sake of clarity only the first 1000 seconds are presented. The inset shows an enlargement at low corrosion currents.

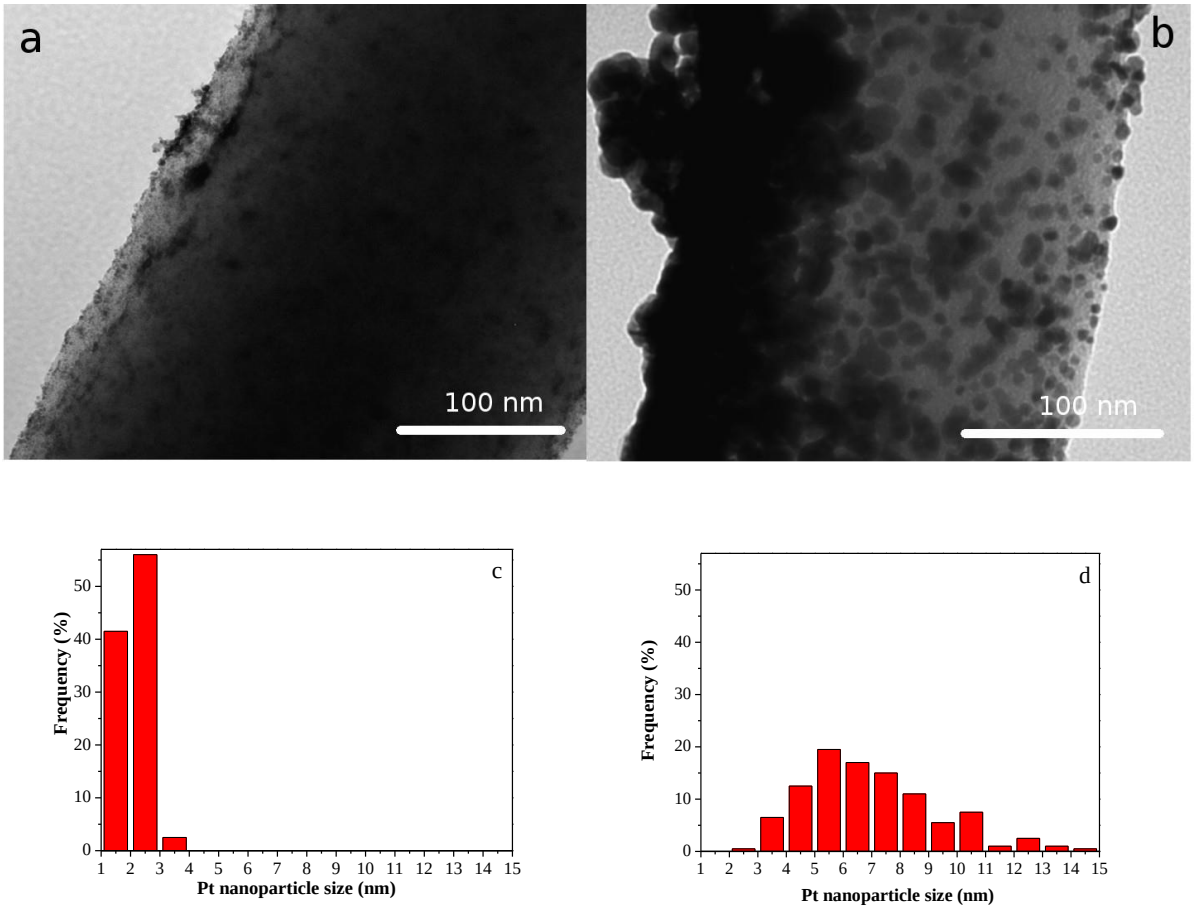

Fig. 6. Transmission electron micrographs of Pt/CNFs before (a) and after voltammetric cycling (b) and corresponding Pt nanoparticle size distribution histograms before (c) and after prolonged cycling (d).

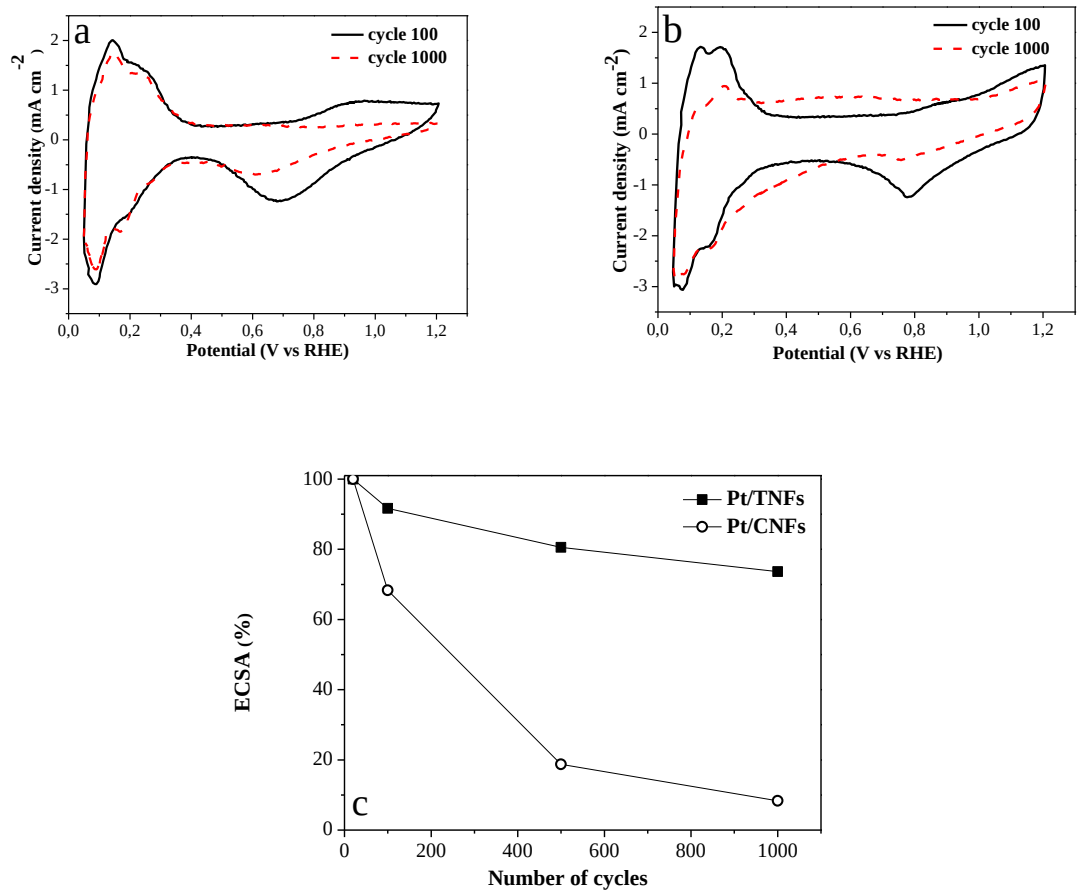

Fig. 7. Cyclic voltammograms after 100 and 1000 cycles on Pt/HTR-TNFs (a) and Pt/CNFs (b) and percentage of retained ECSA of Pt deposited on CNF and HTR-TNFs as a function of number of electrochemical cycles (c).

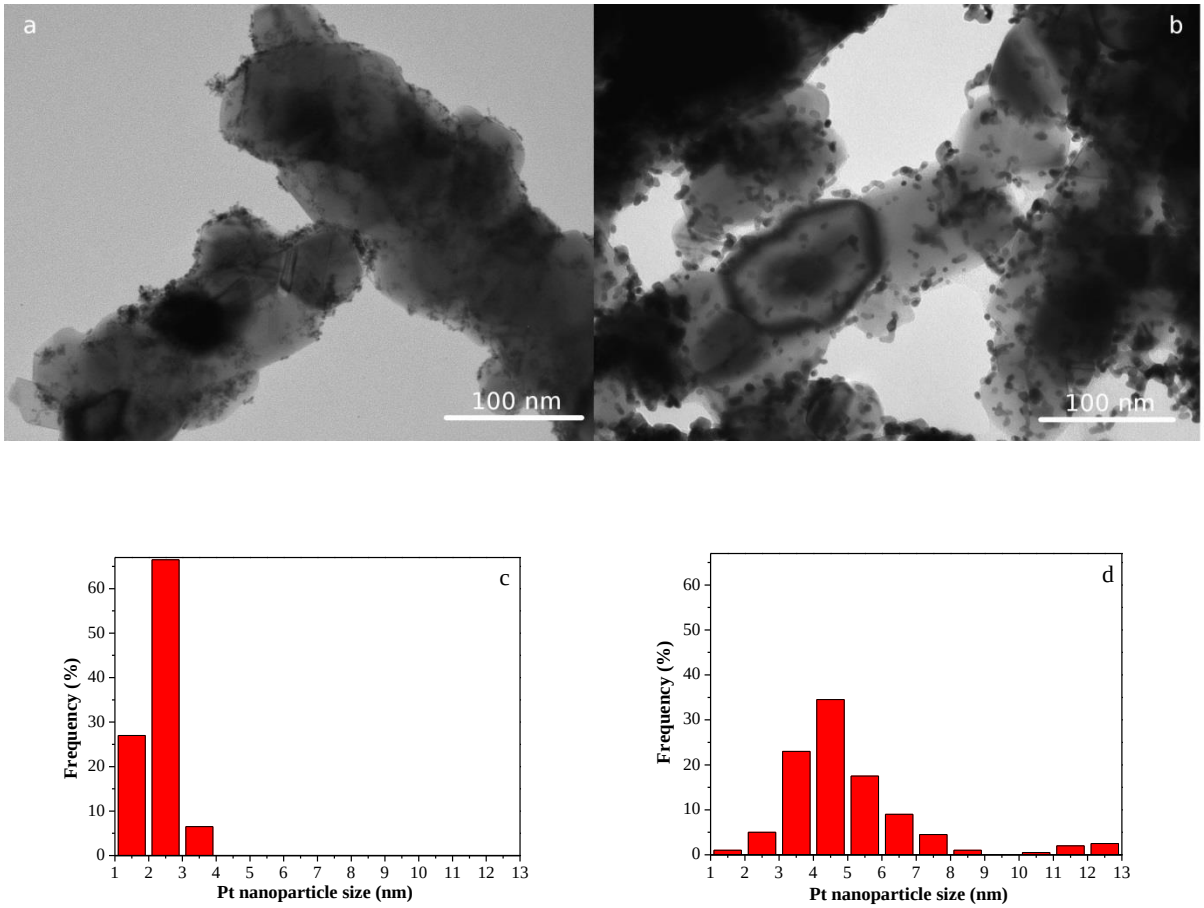

Fig. 8. Transmission electron micrographs of Pt/HTR-TNFs before (a) and after potential cycling (b) and corresponding Pt nanoparticle size distribution histograms before (c) and after prolonged cycling (d).

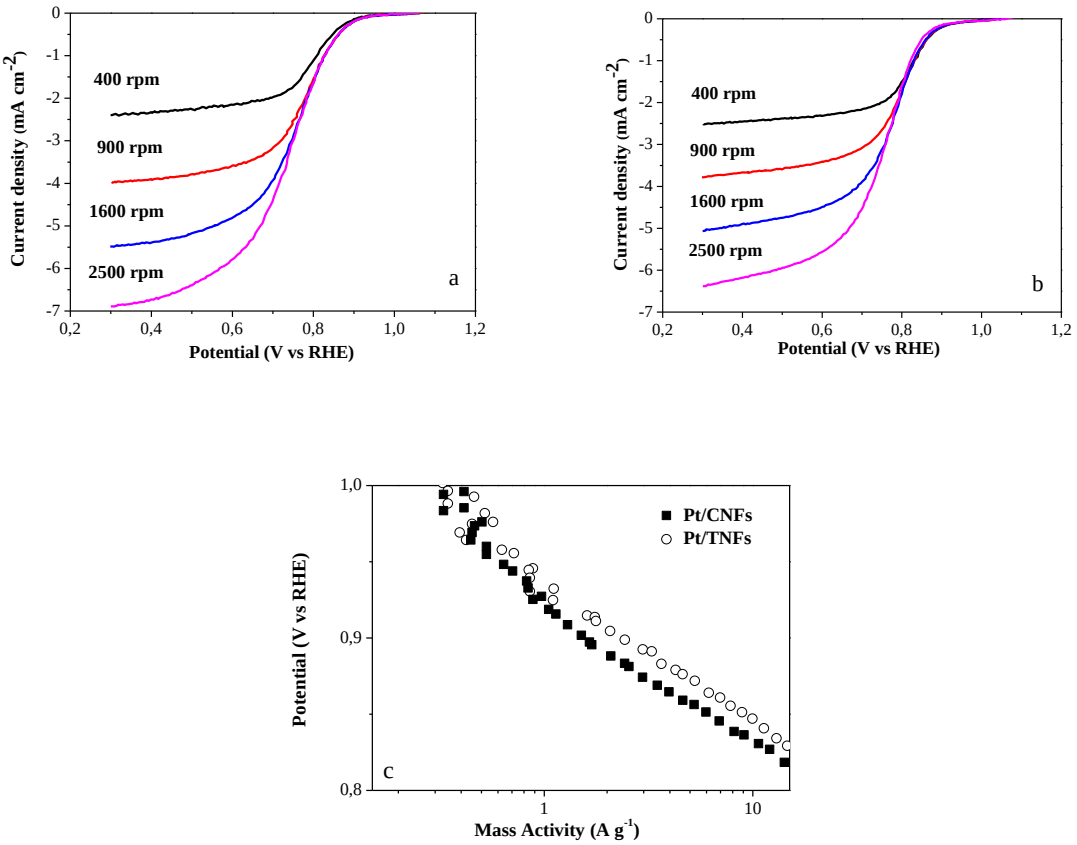

Fig. 9. Oxygen reduction reaction polarisation curves obtained on Pt/HTR-TNFs (a) and Pt/CNFs (b) in O_2-saturated 0.1 M $HClO_4$ at a scan rate of 5 mV s^{-1} at the indicated rotation rates and the corresponding Tafel plots (c). The kinetic current density (activity) was calculated by correcting the cathode current density for O_2-diffusion limitation and normalising it for the Pt loading.

Table 1. Specific surface area (SA, $m^2\ g^{-1}$) and electrical conductivity (σ, S cm^{-1}) at room temperature (RT) for electrospun TNF doped with Nb (0, 5, 10, 20 $\%_{at}$) and treated at different temperatures (LT = 500 °C in air, HT = 800 °C in air, HTR = 800 °C in H_2/Ar).

$\%_{at}$ Nb	**0**			**5**			**10**			**20**		
	LT	HT	HTR	LT	HT	HTR	LT	HT	HTR	LT	HT	HTR
SA	26	15	10	49	15	22	65	22	16	87	19	22
σ	$4{\cdot}10^{-9}$	$6{\cdot}10^{-8}$	$2{\cdot}10^{-5}$	$2{\cdot}10^{-7}$	$2{\cdot}10^{-7}$	$2{\cdot}10^{-3}$	$7{\cdot}10^{-8}$	$2{\cdot}10^{-7}$	$5{\cdot}10^{-3}$	$8{\cdot}10^{-8}$	$9{\cdot}10^{-7}$	$1{\cdot}10^{-3}$

Table 2. Electrochemical surface area and Pt particle size before and after potential cycling between 0.05 and 1.2 V.

Electrocatalyst	**Pt/HTR-TNFs**		**Pt/CNFs**	
	Initial	After 1000 cycles	Initial	After 1000 cycles
ECSA, $m^2\ g^{-1}$	36	27	24	2
Pt nanoparticle size, nm	2.3	5.0	2.3	7.0

Acknowledgements

The research leading to these results has received funding from the Future Emerging Technologies (FET) Programme under the European Community Seventh Framework Programme (FP/2007-2013) under Grant Agreement 256821. The authors gratefully acknowledge this financial support. This work was also funded in part by the French National Research Agency (ANR-12-PRGE-0007).

References

[1] R. Borup, J. Meyers, B. Pivovar, Y.S. Kim, R. Mukundan, N. Garland, D. Myers, M. Wilson, F. Garzon, D. Wood, P. Zelenay, K. More, K. Stroh, T. Zawodzinski, J. Boncella, J.E. McGrath, M. Inaba, K. Miyatake, M. Hori, K. Ota, Z. Ogumi, S. Miyata, A. Nishikata, Z. Siroma, Y. Uchimoto, K. Yasuda, K.-i. Kimijima, N. Iwashita, Chem. Rev., 107 (2007) 3904-3951.
[2] Y.Y. Shao, J. Wang, R. Kou, M. Engelhard, J. Liu, Y. Wang, Y.H. Lin, Electrochim. Acta, 54 (2009) 3109-3114.
[3] B.J. Eastwood, P.A. Christensen, R.D. Armstrong, N.R. Bates, J. Solid State Electrochem., 3 (1999) 179-186.
[4] N. Yousfi-Steiner, P. Moçotéguy, D. Candusso, D. Hissel, J. Power Sources, 194 (2009) 130-145.
[5] X. Wang, W. Li, Z. Chen, M. Waje, Y. Yan, J. Power Sources, 158 (2006) 154-159.
[6] G. Álvarez, F. Alcaide, O. Miguel, P.L. Cabot, M.V. Martínez-Huerta, J.L.G. Fierro, Electrochim. Acta, 56 (2011) 9370-9377.
[7] T. Maiyalagan, Int. J. Hydrogen Energy, 34 (2009) 2874-2879.
[8] R. Sahay, P.S. Kumar, R. Sridhar, J. Sundaramurthy, J. Venugopal, S.G. Mhaisalkar, S. Ramakrishna, J. Mater. Chem., 22 (2012) 12953-12971.
[9] D.H. Reneker, A.L. Yarin, Polymer, 49 (2008) 2387-2425.
[10] S. Cavaliere, S. Subianto, I. Savych, D. J. Jones, J. Rozière, Energy Environ. Sci., 4 (2011) 4761-4785.
[11] W. Zhang, P.N. Pintauro, ChemSusChem, 4 (2011) 1753-1757.
[12] C.-K. Liu, K. Lai, W. Liu, M. Yao, R.-J. Sun, Polym. Int., 58 (2009) 1341-1349.
[13] D. Wang, Y. Liu, J. Huang, T. You, J. Colloid Interface Sci., 367 (2012) 199-203.
[14] Z. Lin, L. Ji, W.E. Krause, X. Zhang, J. Power Sources, 195 (2010) 5520-5526.
[15] Z. Lin, L. Ji, O. Toprakci, W. Krause, X. Zhang, J. Mater. Res., 25 (2010) 1329-1335.
[16] J.-H. Park, Y.-W. Ju, S.-H. Park, H.-R. Jung, K.-S. Yang, W.-J. Lee, J. Appl. Electrochem., 39 (2009) 1229-1236.
[17] E. Antolini, E.R. Gonzalez, Solid State Ionics, 180 (2009) 746-763.
[18] Y.Y. Shao, J. Liu, Y. Wang, Y.H. Lin, J. Mater. Chem., 19 (2009) 46-59.
[19] S. Cavaliere, S. Subianto, I. Savych, M. Tillard, D. J. Jones, J. Rozière, J. Phys. Chem. C, 117 (2013) 18298-18307.
[20] J. Bernard d'Arbigny, G. Taillades, M. Marrony, D. J. Jones, J. Roziere, Chem. Commun., 47 (2011) 7950-7952.
[21] S.J. Tauster, Acc. Chem. Res., 20 (1987) 389-394.

[22] T. Lindgren, J.M. Mwabora, E. Avendaño, J. Jonsson, A. Hoel, C.-G. Granqvist, S.-E. Lindquist, J. Phys. Chem. B, 107 (2003) 5709-5716.
[23] H. Chhina, S. Campbell, O. Kesler, J. Electrochem. Soc., 156 (2009) B1232-B1237.
[24] P.S. Archana, R. Jose, T.M. Jin, C. Vijila, M.M. Yusoff, S. Ramakrishna, J. Am. Ceram. Soc., 93 (2010) 4096-4102.
[25] T.B. Do, M. Cai, M.S. Ruthkosky, T.E. Moylan, Electrochim. Acta, 55 (2010) 8013-8017.
[26] A.M. Ruiz, G. Dezanneau, J. Arbiol, A. Cornet, J.R. Morante, Chem. Mater., 16 (2004) 862-871.
[27] J.-Y. Shin, J.H. Joo, D. Samuelis, J. Maier, Chem. Mater., 24 (2011) 543-551.
[28] S. Siracusano, V. Baglio, C. D'Urso, V. Antonucci, A.S. Aricò, Electrochim. Acta, 54 (2009) 6292-6299.
[29] T. Ioroi, T. Akita, S.-i. Yamazaki, Z. Siroma, N. Fujiwara, K. Yasuda, J. Electrochem. Soc., 158 (2011) C329-C334.
[30] A. Bauer, C. Song, A. Ignaszak, R. Hui, J. Zhang, L. Chevallier, D. Jones, J. Rozière, Electrochim. Acta, 55 (2010) 8365-8370.
[31] S. von Kraemer, K. Wikander, G.R. Lindbergh, A. Lundblad, A.E.C. Palmqvist, J. Power Sources, 180 (2008) 185-190.
[32] S.-Y. Huang, P. Ganesan, B.N. Popov, ACS Catalysis, 2 (2012) 825-831.
[33] L. Chevallier, A. Bauer, S. Cavaliere, R. Hui, J. Rozière, D.J. Jones, ACS Applied Materials & Interfaces, 4 (2012) 1752-1759.
[34] Q. Long, M. Cai, J. Li, H. Rong, L. Jiang, J. Nanopart. Res., 13 (2011) 1655-1662.
[35] A. Bauer, K. Lee, C. Song, Y. Xie, J. Zhang, R. Hui, J. Power Sources, 195 (2010) 3105-3110.
[36] A. Bauer, L. Chevallier, R. Hui, S. Cavaliere, J.J. Zhang, D. Jones, J. Rozière, Electrochim. Acta, 77 (2012) 1-7.
[37] A. Bauer, R. Hui, A. Ignaszak, J. Zhang, D. J. Jones, J. Power Sources, 210 (2012) 15-20.
[38] K. Senevirathne, R. Hui, S. Campbell, S. Ye, J. Zhang, Electrochimica Acta, 59 (2012) 538-547.
[39] F. Fievet, J.P. Lagier, B. Blin, B. Beaudoin, M. Figlarz, Solid State Ionics, 32–33, Part 1 (1989) 198-205.
[40] S. Cavaliere, S. Subianto, L. Chevallier, D. J. Jones, J. Rozière, Chem. Commun., 47 (2011) 6834-6836.
[41] F.C. Nart, W. Vielstich, John Wiley and Sons Inc., Hoboken, NJ, 2003.
[42] N. Yusof, a.F. Ismail, J. Anal. Appl. Pyrolysis, 93 (2012) 1-13.
[43] K.S.W. Sing, D.H. Everett, R.A.W. Haul, L. Moscou, R.A. Pierotti, J. Rouquerol, T. Siemieniewska, Pure Appl. Chem., 57 (1985) 603-619.
[44] C. Kim, S.-H. Park, J.-I. Cho, D.-Y. Lee, T.-J. Park, W.-J. Lee, K.-S. Yang, J. Raman Spectroscopy, 35 (2004) 928-933.
[45] F. Tuinstra, J.L. Koenig, J. Chem. Phys., 53 (1970) 1126-1130.
[46] R. Shannon, Acta Crystallographica Section A, 32 (1976) 751-767.
[47] K. Michalow, D. Flak, A. Heel, M. Parlinska-Wojtan, M. Rekas, T. Graule, Environ. Sci. Pollut. Res., 19 (2012) 3696-3708.
[48] G.Q. Wang, W. Lan, G.J. Han, Y. Wang, Q. Su, X.Q. Liu, J. Alloys Compd., 509 (2011) 4150-4153.
[49] M. Fehse, S. Cavaliere, P.E. Lippens, I. Savych, A. Iadecola, L. Monconduit, D.J. Jones, J. Rozière, F.T. Fischer, C., L. Stievano, J. Phys. Chem. C, 117 (2013) 13827-13835.
[50] S.-Y. Huang, P. Ganesan, B.N. Popov, Applied Catalysis B: Environmental, 96 (2010) 224-231.
[51] O. Frank, M. Zukalova, B. Laskova, J. Kurti, J. Koltai, L. Kavan, PCCP, 14 (2012) 14567-14572.

[52] T. Mazza, E. Barborini, P. Piseri, P. Milani, D. Cattaneo, A. Li Bassi, C.E. Bottani, C. Ducati, Physical Review B, 75 (2007) 045416.
[53] M.Z. Atashbar, H.T. Sun, B. Gong, W. Wlodarski, R. Lamb, Thin Solid Films, 326 (1998) 238-244.
[54] P.M. Kumar, S. Badrinarayanan, M. Sastry, 358 (2000) 122-130.
[55] S.D. Knights, K.M. Colbow, J. St-Pierre, D.P. Wilkinson, J. Power Sources, 127 (2004) 127-134.
[56] P.L. Antonucci, F. Romeo, M. Minutoli, E. Alderucci, N. Giordano, Carbon, 26 (1988) 197-203.
[57] M. Wesselmark, C. Lagegren, G. Lindbergh, ECS Transactions, 25 (2009) 1241-1250.
[58] K. Kinoshita, J. Bett, Carbon, 11 (1973) 237-247.
[59] J.C. Meier, C. Galeano, I. Katsounaros, A.A. Topalov, A. Kostka, F. Schüth, K.J.J. Mayrhofer, ACS Catalysis, 2 (2012) 832-843.
[60] Z. Zhao, L. Castanheira, L. Dubau, G. Berthomé, A. Crisci, F. Maillard, J. Power Sources, 230 (2013) 236-243.
[61] F. Takasaki, S. Matsuie, Y. Takabatake, Z. Noda, A. Hayashi, Y. Shiratori, K. Ito, K. Sasaki, J. Electrochem. Soc., 158 (2011) B1270-B1275.
[62] M. Dou, M. Hou, D. Liang, W. Lu, Z. Shao, B. Yi, Electrochim. Acta, 92 (2013) 468-473.
[63] S.L. Gojković, S.K. Zečević, R.F. Savinell, J. Electrochem. Soc., 145 (1998) 3713-3720.

Supporting Information

On the Effect of Non-Carbon Nanostructured Supports on the Stability of Pt Nanoparticles during Voltage Cycling: a Study of TiO_2 Nanofibres

I. Savych, J. Bernard d'Arbigny, S. Subianto, S. Cavaliere*, D. J. Jones, J. Rozière

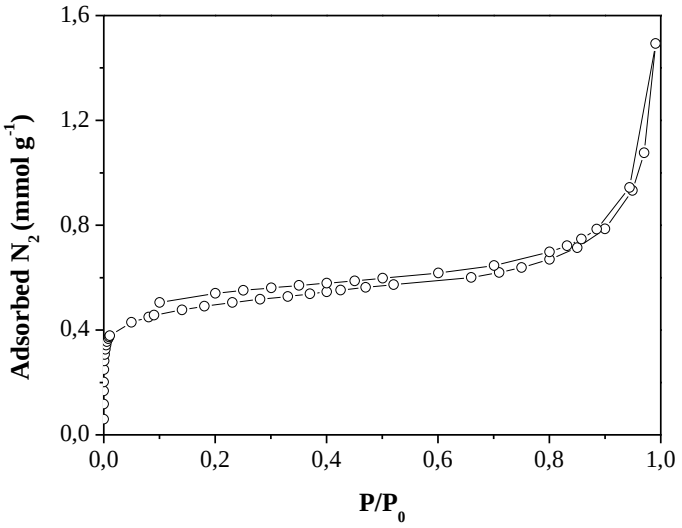

Fig. S1. Nitrogen adsorption-desorption isotherms at -196 °C of carbon nanofibres.

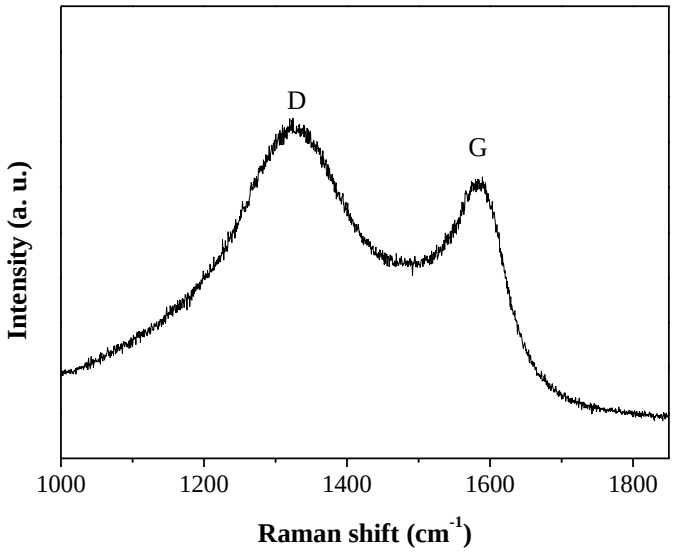

Fig. S2. Raman spectrum of PAN derived electrospun carbon nanofibres.

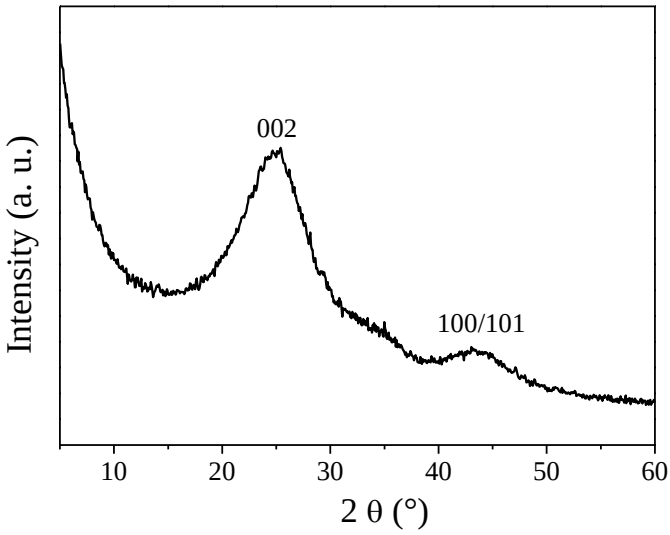

Fig. S3. X-ray diffraction pattern of electrospun carbon nanofibres. (JCPDS 41-1487).

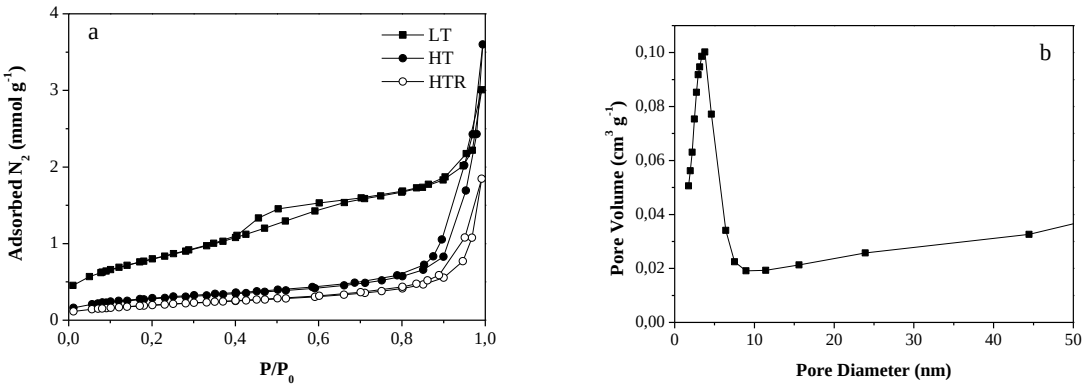

Fig. S4. Nitrogen adsorption-desorption isotherms of 10 % $_{at}$ Nb-TiO_2 nanofibres (a) and pore size distribution for the LT sample (b).

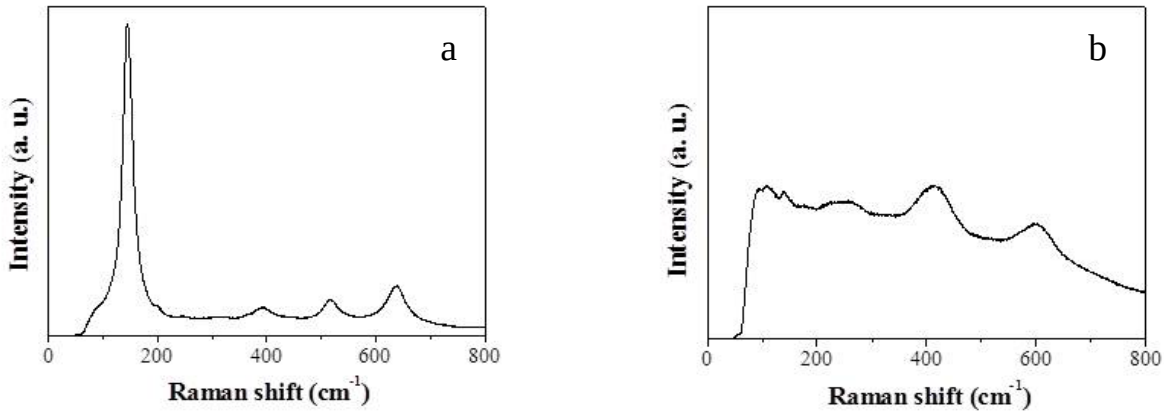

Fig. S5. Raman spectra of 10 $\%_{at}$ Nb-TiO_2 LT (a) and HTR fibres (b).

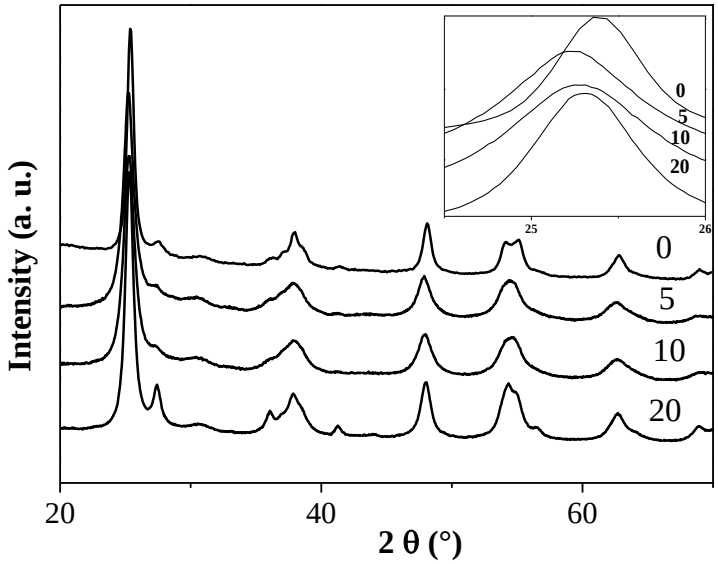

Fig. S6. X-ray diffraction patterns of undoped and 5, 10 and 20 $\%_{at}$ Nb doped titania fibres calcined at 500 °C in air (LR). The inset is a magnification to show the line shift in the 25-26 ° range.

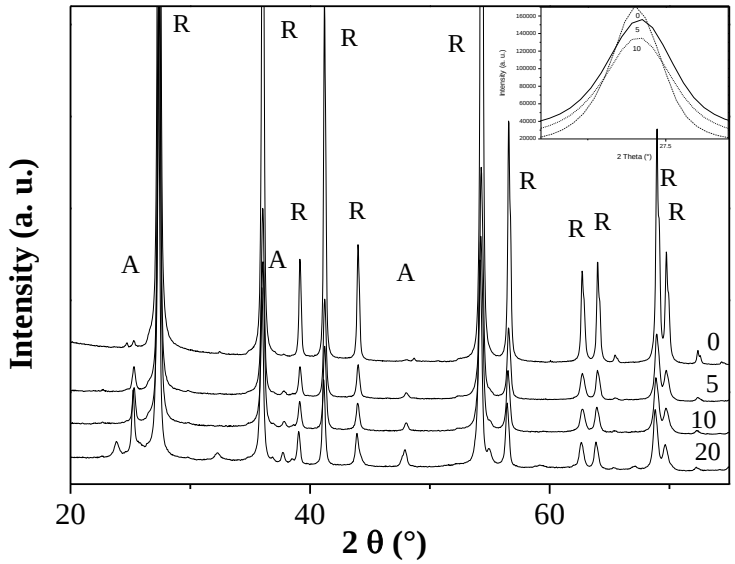

Fig. S7. X-ray diffraction patterns of undoped and 5, 10 and 20 $\%_{at}$ Nb doped titania fibres calcined at 800 °C in air (HT). The inset presents the line shift in the 27-28 ° range.

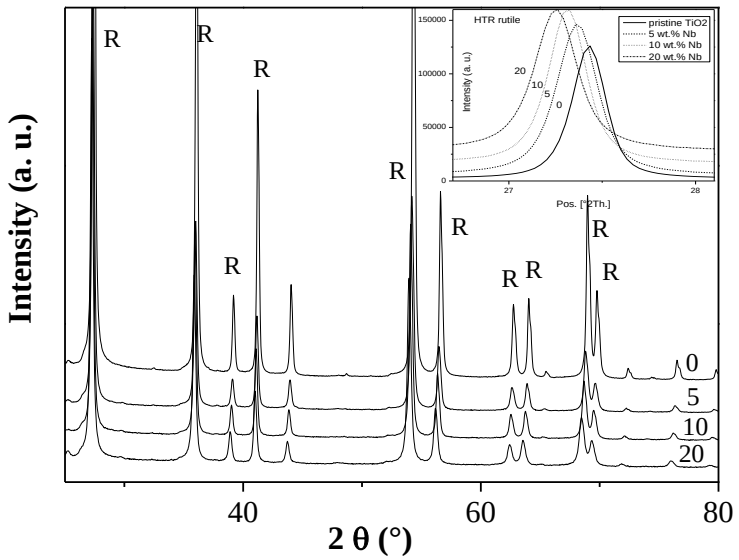

Fig. S8. X-ray diffraction patterns of undoped and 5, 10 and 20 $\%_{at}$ Nb doped titania fibres calcined at 500 °C and then reduced at 800 °C (HTR). The inset presents the line shift in the 27-28 ° range.

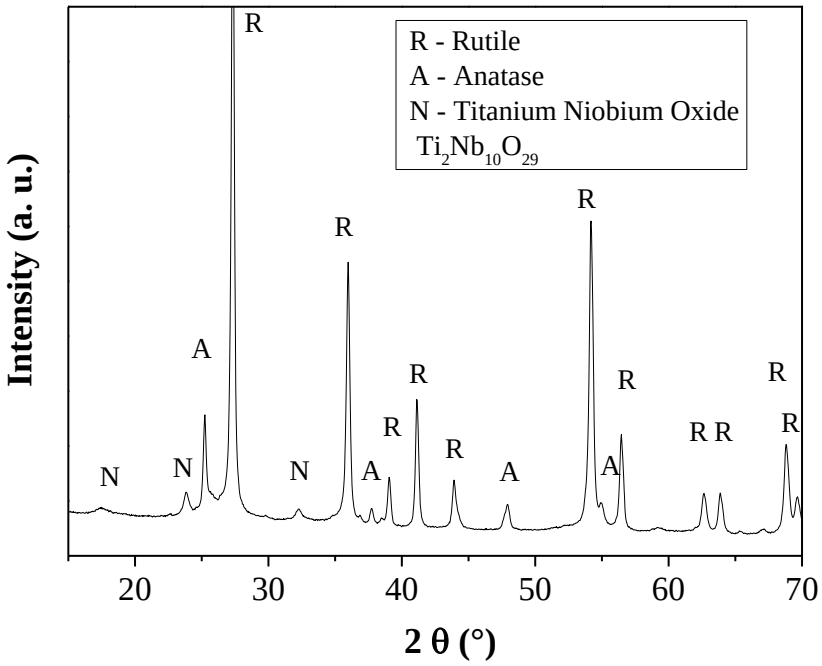

Fig. S9. X-ray diffraction pattern of 20 $\%_{at}$ Nb doped titania fibres calcined at 800 °C.

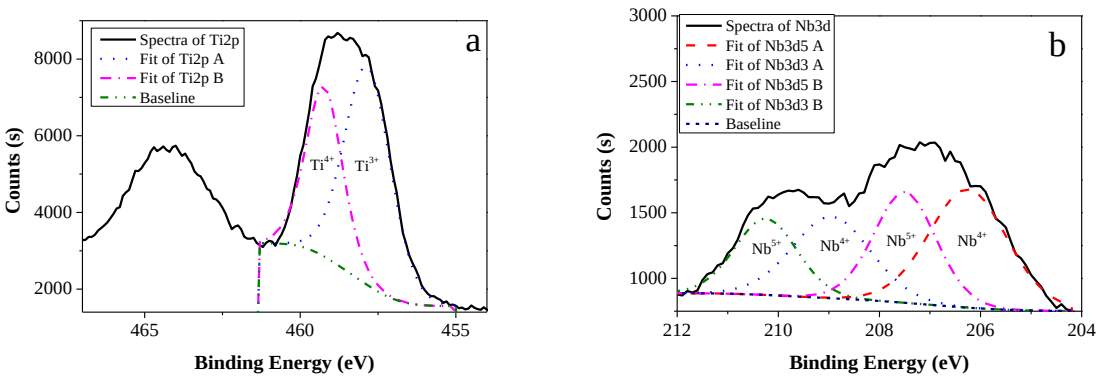

Fig. S10. High resolution XPS spectra of Ti (a) and Nb (b) of the 10 $\%_{at}$ Nb-TiO_2 HTR fibres.

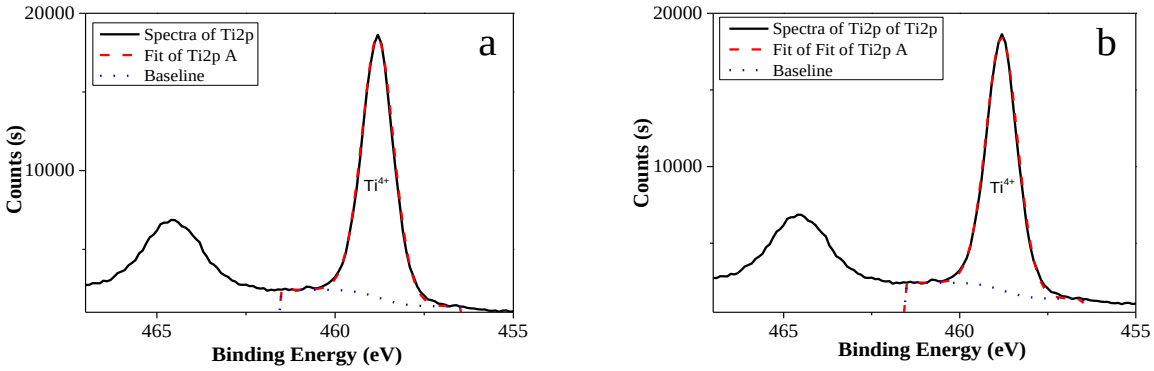

Fig. S11. XPS spectra of Ti for 10 $\%_{at}$ Nb doped titania LT (a) and HT (b).

The Nb 3d spectrum recorded on LT and HT samples showed only a spin-orbit doublet at 207.2 and 209.9 eV that is associated with Nb^{5+} (see SI). However, two contributions are identified in this region of the spectrum given by the HTR sample at 206.2 and 208.9 eV. These signals, attributable to Nb^{4+} [1], correspond to about 57 % of the total niobium content, which implies that Nb^{5+} on the surface of the HTR sample has been reduced by the H_2/Ar thermal treatment.

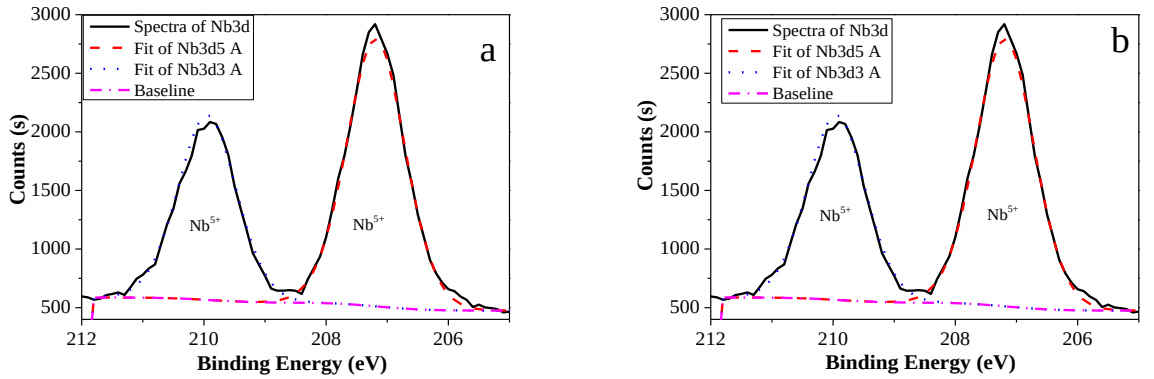

Fig. S12. XPS spectra of Nb for 10 $\%_{at}$ Nb doped titania LT (a) and HT (b).

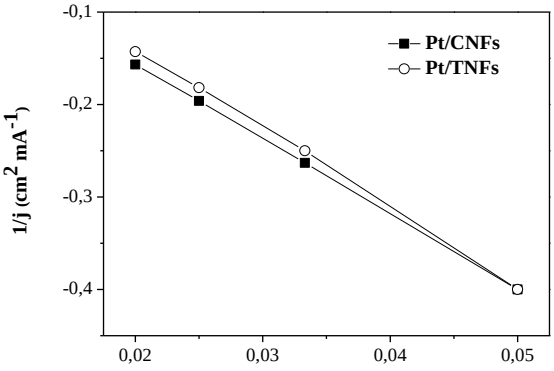

Fig. S13. Levich-Koutecky plot of CNF and HTR-TNF supported Pt at 0.3 V in O_2-saturated 0.1 M $HClO_4$ at a scan rate of 5 mV s^{-1}.

[1] A.M. Ruiz, G. Dezanneau, J. Arbiol, A. Cornet, J.R. Morante, Chem. Mater., 16 (2004) 862-871.